

# An Integrated Deep Learning Model to Analyze CT Scans for Minimally Invasive Accurate Classification of T1a Small Renal Masses

FNU NEHA

Department of Computer Science, Kent State University, Kent, OH, USA; neha@kent.edu

Arvind K. Bansal

Department of Computer Science, Kent State University, Kent, OH, USA; akbansal@kent.edu

Convolution and attention-based deep learning techniques are emerging as promising approaches for automated medical image classification and semantic segmentation for minimally invasive diagnosis of malignant masses in vital organs. However, current deep learning based automated classification techniques are suitable only for detecting renal masses greater than 4.0 cm in diameter, which have a higher probability of malignancy increasing the morbidity, costly disease-management, and the probability of early mortality. T1a Small renal masses (SRM) are less than 4.0 cm in diameter and have a much smaller probability of being malignant and are corrected with partial nephrectomy or ablation. Detection of SRMs poses significant challenges due to low contrast with the surrounding and irregular shapes. As the imaging techniques improve, automated medical image-analysis techniques need further improvement for diagnosing SRMs. In this study, we present an integrated deep learning model and an algorithm for diagnosing T1a SRMs. The model integrates convolution blocks with residual links for capturing local features without information loss, cross-channel attention to focus on important features, principal component analysis to prune low variance features for reduced error and improved computational efficiency, and a transformer-encoder comprising self-attention to maintain dependencies and global context across image-patches. We trained and evaluated our model on the *KiTS19* and *KiTS21* challenge datasets for three ranges {1.2 – 2.0, 2.0 – 3.0, 3.0 – 4.0}. The model achieved an accuracy of 98.1%, 98.5%, and 97.3% for the three ranges, respectively. The accuracy of classification results significantly outperforms other approaches.

**CCS CONCEPTS** • Computational Methodologies → Machine Learning • Applied Computing → Life and Medical Sciences → Healthcare Information Systems

**Additional Keywords and Phrases:** Automated diagnosis, CT scan, deep learning, image processing, kidney, medical image analysis, renal cancer, small renal masses

## ACM Reference Format:

First Author's Name, Initials, and Last Name, Second Author's Name, Initials, and Last Name, and Third Author's Name, Initials, and Last Name. 2018. The Title of the Paper: ACM Conference Proceedings Manuscript Submission Template: This is the subtitle of the paper, this document both explains and embodies the submission format for authors using Word. In Woodstock '18: ACM Symposium on Neural Gaze Detection, June 03–05, 2018, Woodstock, NY. ACM, New York, NY, USA, 10 pages. NOTE: This block will be automatically generated when manuscripts are processed after acceptance.

## 1 INTRODUCTION

Kidneys are a pair of bean-shaped vital organs, each located in the abdomen on either side of the spine, responsible for filtering waste from blood, maintaining pH balance, regulating electrolytes, maintaining blood pressure, and stimulating red blood-cell production by secreting a hormone [1, 2].

Renal cancer - cancer pertaining to kidney, is one of the major causes of kidney malfunction leading to Chronic Kidney Disease (CKD), morbidity, and eventual early mortality [3]. Among the cancer of vital organs, it has the top sixteen mortality rate with 175,000 deaths annually worldwide [2, 4, 5, 6].

Radiographic images, such as ultrasound (US), magnetic resonance imaging (MRI), or computed tomography (CT) (both unenhanced and enhanced), are noninvasive imaging techniques to noninvasively detect renal cancer [7]. Contrast-enhanced ultrasound images (CEUS) are not reliable for detecting *renal masses due* to similar echo-patterns from cancerous tumor cells (RM) [8]. Contrast enhanced CT (CECT) scans are preferred for diagnosing RM due to their effectiveness and lower cost compared to MRI [8, 9].

Most RMs are identified incidentally or at an advanced stage (greater than 4.0 cm) due to the limitations in the lack of human ability to identify small RMs (SRMs) in radiological images and the lack of the visible or pathological symptoms at early stages [10-14]. By that time, the RM has a higher probability of becoming malignant, causing kidney malfunction, morbidity, and early mortality [10-12]. It has been estimated that the increase in the size of tumor by 1 cm increases the probability of malignancy by 16% [10]. Additionally, there is 3% - 5% error (approximately 40 million radiology images every year) by radiologists in diagnosing the radiology images due to fatigue, cognitive problems, and perceptual variations [15]. This error is more for SRMs due to smaller size, low contrast, and irregular shape.

Imaging techniques are continuously improving [9]. As the imaging techniques and the resulting image-resolutions improve, incidental detection of SRM is increasing [11, 12]. Hence, there is a need to improve the automated medical image analysis for automated detection of T1a SRMs, which have low probability of being malignant [11, 12]. Such SRMs can be cured easily at an early stage by partial nephrectomy or ablation without many side-effects and without an increased probability of cancer recurrence [11, 12]. Improved diagnosis would improve patients' prognosis, reduce the cost-burden associated with long-term disease management, and alleviate the impact of workforce shortages in kidney care, especially in developing countries [4, 5].

Three classes of related minimally invasive approaches are being explored to detect solid RMs: (1) Radiomics features analysis [16-18]; (2) pathological biomarkers analysis [19-21]; (3) Machine learning and deep learning based radiology image analysis [22-29], and their partial integrations. Radiomics features analysis extracts limited features from radiology images and combines statistical analysis and classical machine learning for tumors' classification [16-18]. Pathology biomarkers analysis characterizes different classes of tumors based upon a combination of statistical analysis and machine learning of pathology-based biomarkers [19-21]. Deep learning-based approaches are based on the ensembles of convolution networks and attention-based techniques to diagnose different classes of renal tumors [22-29]. Convolution technique detects local spatial features and their hierarchies to understand and classify images [30]. Self-attention techniques capture long-range dependencies between image-patches, providing a global understanding of images [31, 32].

All classes of techniques have their advantages and drawbacks. Radiomics features and pathology biomarker based techniques are limited by known features (or biomarkers) and their specificity, and do not capture all the dependencies between various features. These classes of techniques are in the early stages [33]. Deep learning based image analyses are limited by the resolutions of the imaging devices, a requirement of large databases, and the information-loss during transformations in convolution-based techniques. To alleviate the individual drawbacks, there are recent trends in integrating a subset of these approaches such as machine learning and pathology metadata [34].

Automated classification of stage T1a SRMs (SRMs less than 4.0 cm [11-13]), based on image analysis, remains challenging due to their insufficient contrast with surrounding organs and their irregular shapes [35, 36]. Our research improves deep learning based image analysis techniques. The correlation between various classes of techniques is outside the scope of this paper.

In this research, we develop a model that integrates convolution, residual links (RL) across convolution layers, cross-channel attention (CCA), principal component analysis (PCA) and transformer-encoder (TE) comprising multihead-attention (MHA) to diagnose SRMs in three ranges {1.2 cm – 2.0 cm, 2.0 cm – 3.0 cm, 3.0 cm – 4.0 cm} using the data available in *KiTS 19* and *KiTS 21 challenge datasets* [30-32, 35-39]. Convolutional layers extract local features [30]. RLs across convolution layers mitigate vanishing gradient problem by reducing information loss during convolution [37]. CCA enhances feature representation by selectively emphasizing informative features across different channels. PCA reduces the dimensionality of data and error caused by low variance, while preserving information needed for effective classification [38]. Transformer-encoders (TE) capture long-range dependencies between comprised image-patches [31, 39].

The major contributions of this research are:

1. Application of PCA to reduce data dimensionality and error caused by low variance features;
2. Development of an integrated model based on overall integration of local features, reduction in information loss during transformations using residual links, extracting important features, pruning low variance features, and deriving long-range dependencies;
3. Classifying T1a SRMs between 1.2 cm – 4.0 cm diameter provided in *KiTS challenge datasets*.

The paper is organized as follows: Section 2 presents related studies. Section 3 describes background concepts. Section 4 discusses the proposed architecture and an algorithm. Section 5 describes the implementation. Section 6 discusses the results. Section 7 presents conclusion and future work.

## 2 RELATED WORK

Research efforts to diagnose SRM are classified as radiomics feature analysis, pathology biomarker analysis, deep learning based automated image analysis, and limited combinations of these three classes of techniques.

Pie et al. proposed statistical analysis of a radiomics nomogram that incorporates a radiomics signature and clinical factors for the preoperative differentiation between fat deposits and clear renal cell carcinoma [17]. Nahiri et al. introduced machine learning models (decision tree, random forest, and ADABOOST) to analyze radiomics features to classify benign renal masses from renal cell carcinoma [18].

Rosenkratz et al. analyzed pathological, clinical, and imaging features to assess different renal cell carcinoma types less than 2.0 cm using statistical tests and logistic regression [20]. Mahmud et al. combine the convolution based image analysis with pathological metadata [34].

Previous research on deep learning based analysis has focused on using ensemble methods with pre-trained Deep Neural Network (DNN), Convolution Neural Network (CNN) based systems with decision fusion, and CEUS-based systems integrating CNNs and multi-feature fusion networks (MFFN) [22-29].

Alzu'bi et al. proposed a renal-tumor detection and classification model using an ensemble of techniques: CNN, ResNet50, VGG16. Using the output of this ensemble, images were classified as benign or malignant tumor by another CNN [22]. The drawback of this research is the information-loss that affects their accuracy.

Sudharson et al. proposed an automated classification system using an ensemble of DNNs (*ResNet-101*, *ShuffleNet*, and *MobileNet-v2*) and transfer learning (TL) for feature extraction, followed by classification using a support vector machine (SVM) [23]. The final prediction used majority voting, which has limitations, such as potential bias towards the most frequently predicted model. This limitation reduces performance.

Zabihollahy et al. described an automated classification system to detect solid RMs on CECT images using CNN with decision fusion [24]. Kidney boundaries were detected, cropped to focus on tumor regions, and fed to CNN for the classification between *renal cell carcinoma* (RCC) and benign renal masses. Majority voting was used for the final prediction. This technique also suffers from the limitations of majority-based voting.

Erten et al. integrated Shifted Window (SWIN) and Linear Binary Pattern (LBP) using urine samples to diagnose different renal abnormalities [25, 26]. SWIN, a variant of *vision transformer* (ViT), extracts relevant patches, and LBP extracts features from these patches. SVM was used to select relevant feature-vectors. Final predictions were done using majority voting. Hence, it also suffers from the limitations of majority-based voting.

Wu et al. introduced an ultrasound images based classification system comprising three components: a CNN for feature extraction, an ensemble of object detection techniques (*Single Shot Detector*, *RetinaNet*, and *RefineDet*) to localize kidney regions, and a *multi-feature fusion network* (Mf-Net) for normal and abnormal kidney classification [27]. RetinaNet's ability to support multiple scales, using a *feature pyramid network* (FPN), faces challenges with feature representation and spatial resolution, resulting in excessive false positives.

Choi et al. detected kidney stones using ViT on CT images enhanced by *Super-Resolution CNN* (SRCNN) [28]. Bicubic interpolation, used in SRCNN, blurs high-frequency details, such as edges and textures, leading to a loss in the sharpness and the finer details in the upscaled images. Bicubic interpolation potentially introduces artifacts, such as ringing or halo effects around edges, reducing accuracy.

Kim et al. proposed a machine learning (SVM, logistic regression, k-nearest neighbor (KNN), naïve Bayes (NB), random forest, gradient boost, AdaBoost, and extreme gradient boosting) based prediction model for late recurrence after surgery in patients with renal cell carcinoma [29]. This work does not integrate deep learning techniques of feature extraction with attention or residual connections.

Our model addresses these limitations by integrating a transformer-encoder with convolutional layers and RMs, augmented by CCA and PCA. This integration allows accurate diagnosis of T1a SRMs in the set of ranges {1.2 cm – 2.0 cm, 2.0 cm - 3.0 cm, 3.0 cm – 4.0 cm}, which none of the current image analysis techniques have achieved. As shown in Section 6 (see Table 2), our approach outperforms the accuracy of all other leading deep learning based image analysis models.

### 3 BACKGROUND

A *convolutional-block* is a stack of *convolution-layers* to extract local-features from an input image. Each *convolution-layer* comprises a *convolution-filter* to extract feature-maps [30, 32]. *Rectified Linear Unit* (ReLU) or *Gaussian Error Linear Unit* (GELU) reduce the error from the feature-maps, and a *pooling layer* summarizes the feature-maps.

A *residual link* (RL) is a direct connection to the following convolution layers bypassing one or more intermediate layers [32, 37]. If  $x$  is the output from the  $(i - 1)$ <sup>th</sup> layer, and  $F(x)$  is the output of the  $i$ <sup>th</sup> layer, then input  $H(x)$  for the  $(i + 1)$ <sup>th</sup> layer is equal to  $F(x) + x$ . The direct flow of information  $x$  reduces error in learning and vanishing gradient problem.

A *self-attention* based *TE* comprises a stack of identical layers, each comprising two sub-layers: *MHA* and fully connected *feed-forward network (FFN)*, augmented with *layer normalization (LN)* and *RL*. *TE* captures long-range dependencies and contextual relationships between the image-patches [31, 39]. *MHA* enhances model-efficiency by focusing on the different parts of the input sequence concurrently. Each head has distinct learned weight to compute attention score. These scores are concatenated and linearly transformed to produce the final output.

*Channel attention (CA)* prioritizes important features by computing weights for individual channels through pooling operation followed by *FFN* and a sigmoid function [32]. *CCA* improves *CA* by utilizing direct interactions between each channel and its *k*-nearest neighbors, replacing *FFN* with a convolutional layer.

*Global Average Pooling (GAP)* averages spatial feature-values across the entire spatial dimensions of the feature map [40]. It acts as a global descriptor for each channel [40]. *Batch normalization (BN)* normalizes the spread of the values by taking difference between the values and the mean-value of the batch and dividing by standard deviation of the batch values. It prevents the model from failing to converge and enables higher learning rates.

*PCA* is a multivariate statistical technique for dimensionality reduction [38]. It transforms the original set of dimensions into a new set of orthogonal dimensions in the descending order of their variances. Dimensions with low variances are removed, reducing error in the classification, while preserving the information by keeping high variance features and improving the execution efficiency.

*Gradient-weighted Class Activation Mapping (Grad-CAM)* is a deep learning based visualization technique to highlight the important regions in an input-image [41]. Grad-CAM works by computing the gradient of the class-score after the last convolution layer before a SoftMax layer.

### 3.1 Notations

The symbol  $\oplus$  denotes element-wise addition of two vectors. The symbol  $\otimes$  denotes element-wise multiplication of two vectors.  $Process_1 \rightarrow Process_2$  implies that  $Process_1$  immediately precedes  $Process_2$ . The symbol  $\sigma$  denotes the sigmoid function  $\sigma(x) = 1/(1 + e^{-x})$ . In the equations and figures, for the brevity, we also use *TE* to denote transformer-encoder, *LN* to denote *layer-normalization*, *BN* to denote *batch-normalization*, *RL* to denote *residual link*, *MHA* to denote *multihead-attention*, *PPE* to denote *patch and positional embedding*, and *GAP* to denote *Global Average Pooling*. The variables with superscripts *input* and *output* denote the *input* and *output* for a unit. Subscripts *i*, *j*, and *k* are used to denote the indices in a sequence or stack.

## 4 ARCHITECTURE AND ALGORITHM

The architecture comprises six major components: 1) initial convolution-block; 2) Residual Cross-channel Attention Block (RCCABs); 3) Patch and Position Embedding layer (PPE); 4) stack of TE-blocks; 5) CCA; 6) PCA. GRAD-CAM was used for the visualization of the important regions of interest in the input image. The overall architecture is illustrated in Figure 1. Major components of the architecture are illustrated in Figure 2.

Initial *convolutional-layer* extracts feature-maps from input images. This is followed by *BN*, *ReLU*, and *maxPool* layers. *BN* enhances convergence during learning; *ReLU* reduces noise and introduces non-linearity.

$$FeatureMap = \maxPool(ReLU(BN(conv2D^{16}(inputImage)))) \quad (1)$$

The feature-map  $FeatureMap$  is fed to a *stack of RCCA blocks (RCCAB-stack)* for further processing. *RCCAB-stack* facilitates local-feature extraction (32, 64, 64, 64, 96, 128, 160) using convolution layers, focuses on important features through *CCA*, and mitigates the vanishing gradient problem using RLs. It comprises two *RCCABs (RCCAB-stack  $\rightarrow$  maxPool)*. Each *RCCAB-stack* is a sequence of *RCCAs*.

In our implementation, the stack-size  $m_1$  for the first *RCCAB-stack* is 2, and the stack-size  $m_2$  for the second *RCCAB-stack* is 3. The stack-sizes have been determined empirically, based upon the minimum size that yields maximum accuracy. For the first *RCCA* in the first *RCCAB-stack*, the input vector is the feature-map  $FeatureMap$  from equation (1); for the remaining *RCCAs* within the same stack, the input-vector is the output-vector from the previous *RCCA*.

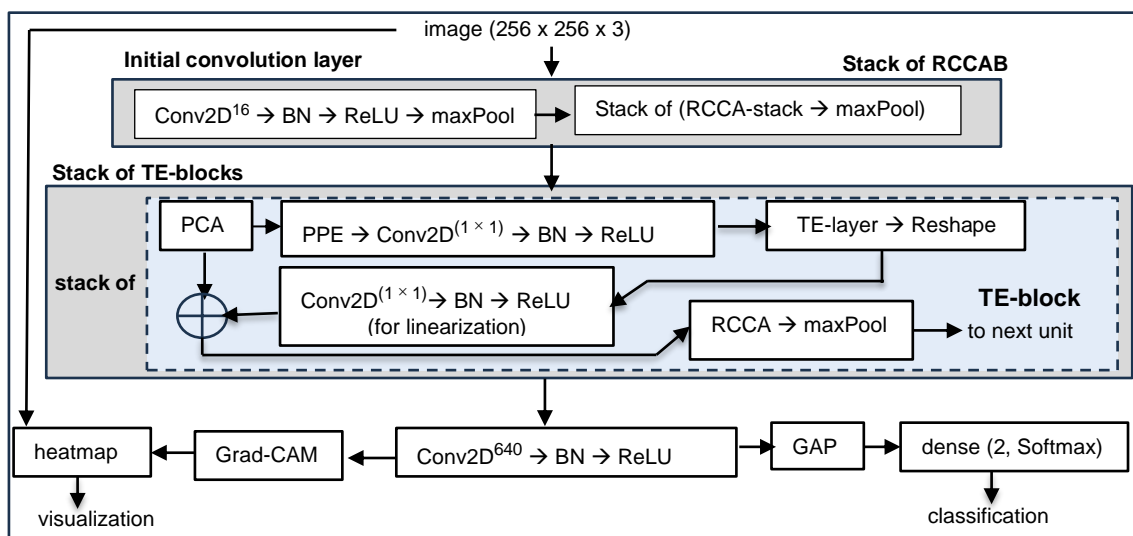


Figure 1: A schematic of overall architecture

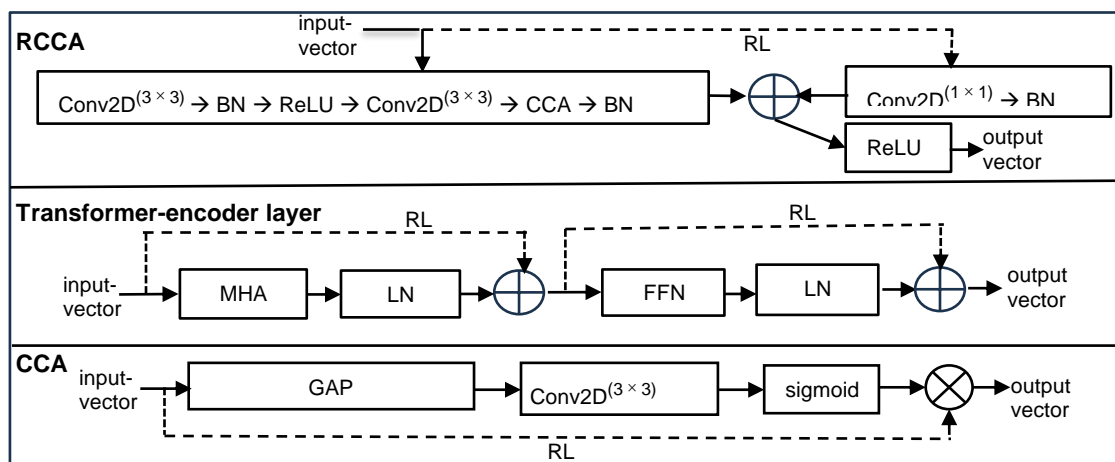


Figure 2: Components of the proposed architecture

Each *RCCA* begins with a  $\text{Conv2D}^{(3 \times 3)}$  layer, followed by *BN*, *ReLU* and another  $\text{Conv2D}^{(3 \times 3)}$  layer, to learn spatial features from the input data. The output is then passed to a *CCA*. A *CCA* employs *GAP* followed by  $\text{Conv2D}^{(3 \times 3)}$  and sigmoid function  $\sigma$ . *GAP* extracts global descriptors of each feature-map.  $\text{Conv2D}^{(3 \times 3)}$  establishes correspondence within the windows of *GAP-values*. The sigmoid function  $\sigma$  maps the output of *GAP-values* to the range [0.0, 1.0]. Feature-maps mapping close to 1.0 have higher importance.

The architecture of *RCCAB* is summarized in equations (2)-(6). The input to *CCA* is given by equation (2). The output of *CCA* is given by equation (3). The output of *RCCA* is given by equation (4). The output of *maxPool*, fed to the next *RCCA*-unit, is given by equation (5). The final output  $RCCAB^{output}$  is given by equation (6), where  $n$  is the index of the last *maxPool* unit. In our architecture  $n = 2$ . The index  $i$  denotes the stack-index; the index  $j$  denotes the index of *RCCA* in the  $i$ th *RCCA-stack*;  $m$  denotes the number of *RCCAs* in an *RCCA-stack*.

$$CCA_{ij(1 \leq j \leq m)}^{input} = \text{Conv2D}^{(3 \times 3)}(\text{ReLU}(\text{BN}(\text{Conv2D}^{(3 \times 3)}(RCCA_{ij(1 \leq j \leq m)}^{input})))) \quad (2)$$

$$CCA_{ij(1 \leq j \leq m)}^{output} = CCA_{ij(1 \leq j \leq m)}^{input} \otimes (\sigma(\text{conv2D}^{(3 \times 3)}(\text{GAP}(CCA_{ij(1 \leq j \leq m)}^{input})))) \quad (3)$$

$$RCCA_{i(j+1)}^{input} = RCCA_{ij(1 \leq j \leq m)}^{output} = \text{ReLU}(\text{BN}(CCA_{ij(1 \leq j \leq m)}^{output}) \oplus \text{BN}(\text{Conv2D}^{(1 \times 1)}(RCCA_{ij(1 \leq j \leq m)}^{input}))) \quad (4)$$

$$RCCA_{(i+1)1(1 \leq i+1 \leq n)}^{input} = \text{maxPool}(RCCA_{im}^{output}) \quad (5)$$

$$RCCAB^{output} = \text{maxPool}(RCCA_{nm}^{output}) \quad (6)$$

$RCCAB^{output}$  is fed to the first *TE-block* in the *stack of TE-blocks*. The stack-size is 3 in our implementation. Each block captures long-range dependencies and global context across feature-maps. It comprises 1) *PCA layer* to prune low-variance features; 2) *PPE* for dividing  $PCA_i^{output}$  into non-overlapping patches; 3) *TE layer* to derive long-range dependencies among features; 4) a  $\text{conv2D}^{(1 \times 1)}$  layer for linearization; 5) an *RCCA layer* for the extraction of important features.

Prior to feeding data into the next *TE-layer*, *PCA* is applied. The input for *PCA* layer in the first *TE-block* is  $\text{maxPool}(RCCAB^{output})$ . In the subsequent *PCAs*, the input is the output of the previous *TE-block's* (*RCCA*  $\rightarrow$  *maxPool* layer). The inputs for *PCA* layers are given by the equations (7)-(8). The output from the *PCA* layers is given by equation (9). The index  $k$  ( $1 \leq k \leq 3$ ) denotes the index of the current *TE-block* being processed.

The *PPE* layer occurs before the *TE-layer*. *PPE* divides  $PCA_i^{output}$  into non-overlapping patches. Each patch is passed through a  $\text{conv2D}^{(1 \times 1)}$  to obtain the *PPE-vector* of size  $1 \times P$ , where  $P$  is *patch-size*  $\times$  *patch-size*. *PPE-vector* is augmented with *learned positional embedding*  $LPE^{(N \times D)}$  to retain spatial information.  $LPE^{(N \times D)}$  is a trainable matrix of size  $(N, D)$ , where  $N$  denotes the number of patches, and  $D$  is the embedding-dimension (144, 192, 240). The value of  $N$  is calculated as  $(H \times W) / P$ , where  $H$  and  $W$  denote the height and width of the input feature-map, respectively. This matrix is initialized randomly and learned during training. After deriving the embeddings, input to the *TE-layer* is given by the equation (10).

*TE-layer* utilizes *RLs* (see Figure 2) to ensure that the information is not lost. *TE-layer* uses a combination of *MHA*, *RL*, *FFN* to derive the dependencies in the feature-map. The normalized *MHA*-output  $MHA^{output}$  is given by the equation (11). After processing through the encoders, the tensor is reshaped to its original spatial dimensions. The reshaped output of the *TE-layer* is given by the equation (12).

$$PCA_1^{input} = RCCAB^{output} \quad (7)$$

$$PCA_{i+1(1 \leq i \leq k-1)}^{input} = \text{maxPool}(RCCA_2^{output}); \quad (8)$$

$$PCA_i^{output} = PCA(PCA_i^{input}) \quad (9)$$

$$TE_{i(1 \leq i \leq k)}^{input} = ReLU(BN(Conv2D^{(1 \times 1)}(PPE(PCA_i^{output}) \oplus LPE^{(N \times D)}))) \quad (10)$$

$$MHA_{i(1 \leq i \leq k)}^{output} = TE_{i(1 \leq i \leq k)}^{input} \oplus LN(MHA(TE_{i(1 \leq i \leq k)}^{input})) \quad (11)$$

$$TE_{i(1 \leq i \leq k)}^{output} = Reshape(LN(FFN(MHA_{i(1 \leq i \leq k)}^{output}))) \oplus MHA_{i(1 \leq i \leq k)}^{output} \quad (12)$$

The reshaped encoder-output  $TE_{i(1 \leq i \leq k)}^{output}$  is fed to linearization-layer comprising ( $Conv2D^{(1 \times 1)} \rightarrow BN \rightarrow ReLU$ ) to linearize the output  $TE_{i(1 \leq i \leq k)}^{output}$ .  $Conv2D^{(1 \times 1)}$  layer expands the tensor back to its original number of channels.  $Linear_{i(1 \leq i \leq k)}^{output}$  – the output of this *linearization layer* is given by the equation (13). The linearized output  $Linear_{i(1 \leq i \leq k)}^{output}$  is element-wise added to the PCA output  $PCA_i^{output}$  to derive input to the following *RCCA*-layer  $RCCA2_i^{input}$  as shown in the equation (14).

$$Linear_{i(1 \leq i \leq k)}^{output} = ReLU(BN(Conv2D^{(1 \times 1)}(TE_{i(1 \leq i \leq k)}^{output}))) \quad (13)$$

$$RCCA2_{i(1 \leq i \leq k)}^{input} = PCA_i^{output} \oplus Linear_{i(1 \leq i \leq k)}^{output} \quad (14)$$

After processing the final *TE-block*,  $RCCA2_3^{output}$  – the final output of the stack of the *TE-blocks*, is fed to a convolutional-block ( $Conv2D^{640} \rightarrow BN \rightarrow ReLU$ ) that extracts 640 feature-maps to adjust channel dimensions, followed by *GAP* to distill the spatial information. Finally, a dense layer with *softmax* function derives the probabilities of various classes for the given image. The *arg\_max* function picks the most probable class. The final output class is given by the equation (15). The overall algorithm is described in Algorithm 1.

$$Class = arg\_max(softmax(ReLU(BN(Conv2D^{640}(RCCA2_3^{output})))))) \quad (15)$$

## 5 IMPLEMENTATION

The software was developed using Python 3.9, using the TensorFlow framework V2.16.1. The model was trained on a single processor in a processor-cluster, accelerated by an NVIDIA Tesla V100 GPU and 32 GB of RAM, supported by CUDA 11.8.0, and cuDNN version 8801. The process took 8 hours to complete on this machine, with an average epoch time of 84.3 seconds. Each epoch processed 214 images.

### 5.1 Data and Preprocessing

Publicly available *KiTS19* and *KiTS21 Challenge datasets* were used [35, 36] to train, validate, and test our model. The extracted datasets contained axial projections of 300 contrast-enhanced annotated CT scans, each containing 512 image-frames, obtained from patients who underwent partial or radical nephrectomy for kidney tumors. Ground truth labels were manually annotated and confirmed by expert clinicians.

All image-frames were converted into JPG format, resulting in 153,560 images (300 X 512). After filtering out black images, 23,100 images, displaying anatomical organs, were retained. From these, 13,579 images had tumor size less than 4.0 cm, which included tumor-sizes in the range of {1.2 cm - 2.0 cm, 2.0 cm – 3.0 cm, 3.0 cm – 4.0 cm}. Clinical annotations showed 10,327 images of healthy kidney and 3,252 images having SRMs. These images were selected for the experiment.

The images were resized to 256 x 256 pixels using nearest-neighbor interpolation to preserve sharp edges and other details. Intensity values were normalized using min-max scaling to map in the range [0.0, 1.0]. *Synthetic Minority Over-sampling Technique* (SMOTE) was used to create synthetic samples for the minority

class by interpolating between existing samples [42]. SMOTE generates new samples along the line segments connecting the instance to its neighbors. This process resulted in 10,327 SRM images and a total of 20,654 images. Our model was trained on 20,654 images. Sample images are shown in Figure 3.

---

ALGORITHM 1 – A deep learning algorithm to accurately classify SRM and healthy kidney

---

**Algorithm** classify\_SRM

**Input:** 1. image-frame  $Im$ ; 2. number of RCCA stacks  $n$ ; 3. sequence of RCCA stack-sizes  $\{m_1, \dots, m_n\}$   
4. transformer-encoder stack-size  $k$ ;

**Output:** 1. classification pair  $(Im, class)$ , where  $class \in \{healthy, SRM\}$

```
{ Feature-map  $FM = \maxPool(ReLU(BN(conv2D^{16}(Im))))$ ; % apply equation (1) to derive initial feature-map
   $i = 1$ ;  $RCCA_{i1}^{input} = FM$ ; % feed initial feature-map to first RCCA in the first RCCA-stack
  while ( $i < n$ ) % process stack of RCCAB
    {  $m = m_i$ ;  $j = 1$ ; % Initialize
      while ( $j \leq m$ ) % process  $i$ th RCCA in  $i$ th RCCAB
        {  $CCA_{ij}^{input} = Conv2D^{(3 \times 3)}(ReLU(BN(Conv2D^{(3 \times 3)}(RCCA_{ij}^{input}))))$ ; % Apply equation (2)
           $CCA_{ij}^{output} = CCA_{ij}^{input} \otimes (\sigma(conv2D^{(3 \times 3)}(GAP(CCA_{ij}^{input}))))$ ; % Apply equation (3)
          % Apply equation (4) to compute  $RCCA_{i(j+1)}^{input} = RCCA_{ij}^{output}$ 
           $RCCA_{i(j+1)}^{input} = RCCA_{ij}^{output} = ReLU(BN(CCA_{ij}^{output}) \oplus BN(Conv2D^{(1 \times 1)}(RCCA_{ij}^{input})))$ ;
           $j = j + 1$ ; } % Increment the index to process the next RCCA layer
         $i = i + 1$ ;  $RCCA_{i1}^{input} = \maxpool(RCCA_{im}^{output})$ ; } % Apply equation (5) and go to next RCCAB
     $RCCAB^{output} = \maxpool(RCCA_{nm}^{output})$ ; % Apply equation (6) to derive the final output of RCCAB-stack
     $PCA_1^{input} = RCCAB^{output}$ ;  $i = 1$ ; % Apply equation (7) to feed the data to the stack of transformer-encoder block
    while ( $i \leq k$ ) % Process the transformer-encoder block (TE-block)
      {  $PCA_1^{output} = PCA(PCA_1^{input})$ ; % Apply PCA for the first time
         $TE_{i(1 \leq i \leq k)}^{input} = ReLU(BN(Conv2D^{(1 \times 1)}(PPE(PCA_i^{output}) \oplus LPE^{(N \times D)})))$  % Apply equation (10)
         $MHA_{i(1 \leq i \leq k)}^{output} = TE_{i(1 \leq i \leq k)}^{input} \oplus LN(MHA(TE_{i(1 \leq i \leq k)}^{input}))$ ; % Apply equation (11)
         $TE_i^{output} = Reshape(LN(FFN(MHA_i^{output}))) \oplus MHA_i^{output}$ ; % Apply equation (12)
         $Linear_i^{output} = ReLU(BN(Conv2D^{(1 \times 1)}(TE_i^{output})))$ ; % Apply equation (13) for linearized output
         $RCCA2_i^{input} = PCA_i^{output} \oplus Linear_i^{output}$ ; % Apply equation (14) to feed linearized output to second RCCA
         $CCA2_i^{input} = Conv2D^{(3 \times 3)}(ReLU(BN(Conv2D^{(3 \times 3)}(RCCA2_i^{input}))))$ ; % Apply equation (2) within RCCA2
         $CCA2_i^{output} = CCA2_i^{input} \otimes (\sigma(conv2D^{(3 \times 3)}(GAP(CCA2_i^{input}))))$ ; % Apply equation (3) within RCCA2
         $RCCA2_i^{output} = ReLU(BN(CCA2_i^{output}) \oplus BN(Conv2D^{(1 \times 1)}(RCCA2_i^{input})))$ ; % Apply equation (4) within RCCA2
         $PCA_{i+1}^{input} = RCCA2_i^{output}$ ;  $i = i + 1$ ; } % Increment the index and go to the following layer in the TE-blocks stack
     $Class = \arg\_max(\text{softmax}(ReLU(BN(Conv2D^{640}(RCCA2_k^{output}))))))$ ; % Apply equation (15) to derive the class
  }
  return ( $Im, Class$ ); }
```

---

## 5.2 Training

The dataset was split into training, validation, and test sets, including 12,392 (60%), 4130 (20%), and 4132 (20%) samples, respectively. The classification model was trained for 200 epochs, based upon the highest stable accuracy experiment with the minimum number of epochs (see Figure 4a), with additional five-fold cross-validation to mitigate overfitting.

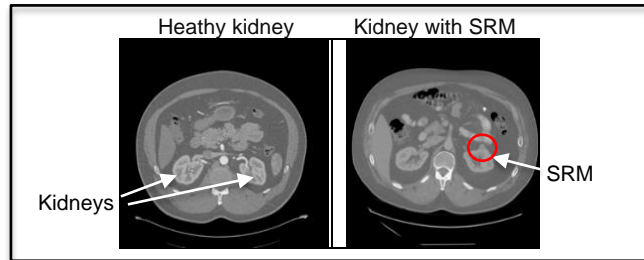


Figure 3: Sample CT axial slices showing a healthy kidney and kidney with SRM from public domain *KiTS* datasets [35, 36]

The training employed *Adaptive Moment Estimation with Weight Decay* (AdamW) optimizer, configured with a learning rate of 0.001 and weight decay of 0.0001. A batch-size of 16 was used for efficient gradient computation. The categorical cross-entropy loss-function was utilized for loss computation. Throughout the training and evaluation, the model's performance was assessed using categorical accuracy metrics, which measure the proportion of correctly predicted labels across all classes.

## 6 RESULTS AND DISCUSSION

The model's performance was evaluated using confusion matrix, accuracy, precision, F1-score, sensitivity, and specificity on a set of 4132 (1139 in SRM-range 1.2 cm - 2.0 cm; 1873 in SRM-range 2.0 cm - 3.0 cm; 1120 in SRM-range 3.0 cm - 4.0 cm) randomly selected images (see Table 1). The performance data showed an accuracy of 97.6% for the SRM-range 1.2 cm - 2.0 cm; an accuracy of 98.5% for the SRM-range 2.0 to 3.0 cm; an accuracy of 97.3% for the SRM-range 3.0 to 4.0 cm.

Table 1: Evaluation metrics for classification

	Confusion matrix		Other evaluation metrics				
	Healthy kidney	SRM kidney	Accuracy	Specificity	Precision	F1-score	Sensitivity
Healthy kidney	551	8	98.1%	97.7%	97.5%	97.9%	98.6%
SRM $\leq$ 2.0 cm	14	566	98.1%	98.6%	98.5%	98.1%	97.7%

Most of the related work has focused on reporting accuracy as the performance metrics for their models. We provide a more comprehensive evaluation by including accuracy, precision, F1-score, sensitivity, and specificity.

Table 2 presents a comparison of our model with kidney-related disease classification models. Other models cannot diagnose SRM less than 4.0 cm. Our model accurately detects SRM at least in the range 1.2 cm – 4.0 cm as available in the *KiTS 19* and *KiTS 21 challenge datasets* [35, 36]. Our model significantly outperforms the accuracy achieved by other models. Figure 4 illustrates our experimental results.

Table 2: Comparison with other models classifying renal masses

Model	Accuracy	Model	Accuracy
[22] Dalia et al.: CNN + ResNet + VGG	92.0%	[27] Wu et al.: CNN + MF-net + Pyramid	94.7%
[23] Sudarsh. et al.: DNN + TL + SVM + voting	96.5%	[28] Choi et al.: SRCNN + ViT	93.0%
[24] Zabihollahy et al.: CNN + decision fusion	83.8%	[29] Kim et al.: Machine Learning	79.9%
[25] Erten et al.: SWIN + LBP + voting	92.6%	<b>Our integrated model</b>	<b>98.1%</b>

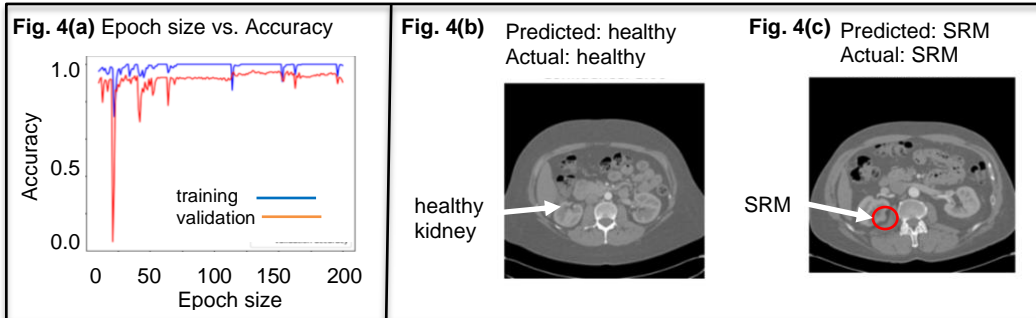


Figure 4: Experimental results for accuracy in classification. Fig. 4(a) shows the training and validation accuracy. Fig. 4(b) shows the prediction of healthy kidney classification. Fig. 4(c) shows the prediction of SRM in a kidney. Accuracy progressively stabilizes after 200 epochs. Figures 4(b) and 4(c) are adopted from *KiTS* datasets in public domain [35, 36].

## 7 CONCLUSION AND FUTURE WORK

Early-stage automated diagnosis of SRM will avoid undesired malignancy, improve patient prognosis, and reduce morbidity and long-term cost burden. We have proposed an integrated deep learning model to detect SRM in a set of diameter-ranges {1.2 cm – 2.0 cm, 2.0 cm – 3.0 cm, 3.0 cm – 4.0 cm} with high accuracy. The model integrates local features, global interdependencies, reduces information loss, mitigates vanishing gradient problem, and uses PCA based dimension-reduction for pruning low variance features.

Currently, our model has been tested, based upon the availability of the test data in *KiTS 19* and *KiTS 21 challenge dataset*, to classify SRMs greater than 1.2 cm from axial slices [35, 36]. It could not be tested below 1.2 cm diameter due to the unavailability of data in the datasets. The current approach does not utilize the information available from coronal and sagittal axes slices.

Our model currently classifies cases into binary categories: healthy kidney and SRM  $\leq 2$  cm, healthy kidney and SRM  $\leq 3$  cm, or healthy kidney and SRM  $\leq 4$  cm. It does not handle multi-class cases where it needs to differentiate between healthy kidney and SRM within range 1.2 – 2.0, 2.0 – 3.0, 3.0 – 4.0 simultaneously. We plan to implement the multiclass classification in the future.

We intend to perform multi-axial analysis by integrating data from *coronal* and *sagittal* views and tumor heterogeneity patterns, including correlation with biopsy images, and correlation with pathological outcomes to improve accuracy and subclassify renal tumor types [34, 43].

## ACKNOWLEDGMENTS

We thank Ohio Supercomputing Center (OSC) for the use of supercomputing cluster to train our model through an educational grant.

## REFERENCES

- [1] Alexandre Coffin, Isabelle Boulay-Coletta, Delphine Sebbag-Sfez, and Marc Zins. 2015. Radioanatomy of the retroperitoneal space. *Diagnostic and Interventional Imaging* 96, 2 (February 2015), 171-86. <https://doi.org/10.1016/j.diii.2014.06.015>
- [2] Helmut G. Rennke and Bradley M. Denker. 2019. *Renal Pathophysiology: The Essentials*, 5th ed., Lippincott Williams & Wilkins
- [3] Bénédicte Stengel. 2010. Chronic kidney disease and cancer: a troubling connection. *J. Nephrol* 23, 3 (May-June 2010), 253-262. <https://pubmed.ncbi.nlm.nih.gov/20349418>
- [4] International Agency for Research on Cancer, World Health Organization. Cancer today: kidney cancer factsheet. Retrieved July 17, 2024, <https://gco.iarc.who.int/media/globocan/factsheets/cancers/29-kidney-fact-sheet.pdf>

- [5] Freddie Bray, Mathieu Laversanne, Hyuna Sung, Jacques Ferlay, Rebecca L. Siegel, Isabelle Soerjomataram, and Ahmedin Jamal. 2024. Global cancer statistics 2022: GLOBOCON estimates of incidence and mortality worldwide for 36 cancers in 185 countries. *CA cancer J Clin* 74, 229-263. <https://doi.org/10.3322/caac.21834>
- [6] Aminu K. Bello, Ikechi G. Okpechi, Adeera Levin, Feng Ye, Sandrine Damster, Silvia Arruebo, et al. 2024. An update on the global disparities in kidney disease burden and care across world countries and regions. *The Lancet Global Health* 12, 3 (March 2024), E382-E395. [https://doi.org/10.1016/S2214-109X\(23\)00570-3](https://doi.org/10.1016/S2214-109X(23)00570-3)
- [7] Michael J. Leveridge, Peter J. Bostrom, George Koulouris, Antonio Finelli, and Nathan Lawrentschuk. 2010. Imaging renal cell carcinoma with ultrasonography, CT and MRI. *Nat Rev Urol* 7, 6 (June 2010), 311–325. <https://www.nature.com/articles/nrurol.2010.63>
- [8] Tim J. Van Oostenbrugge, Jurgen J. Fütterer, and Peter F. A. Mulders. 2018. Diagnostic imaging for solid renal tumors: a pictorial review. *Kidney Cancer* 2, 2 (August 2018), 79-93. <https://doi.org/10.3233/KCA-180028>
- [9] Daniel T. Ginat and Rajiv Gupta. 2014. Advances in computed tomography imaging technology. *Annu. Rev. Biomed. Eng* 16 :431–453. <https://doi.org/10.1146/annurev-bioeng-121813-113601>
- [10] R. Houston Thompson, Jordan M. Kurta, Matthew Kaag, Satish K. Tickoo, Shilajit Kundu, Darren Katz, et al. 2009. Tumor size is associated with malignant potential in renal cell carcinoma cases. *J. Urol* 181, 5 (May 2009), 2033–36. <https://doi.org/10.1016/j.juro.2009.01.027>
- [11] Dena Moskowitz, Jenny Chang, Argyrios Ziogas, Hoda Anton-Culver, and Ralph V. Clayman. 2016. Treatment for T1a renal cancer substratified by size: less is more. *J. Urol* 196, 4 (October 2016), 1000-1007. <https://doi.org/10.1016/j.juro.2016.04.063>
- [12] Alejandro Sanchez, Adam S. Feldman, and Abraham Ari Hakimi. 2018. Current management of small renal masses, including patient selection, renal tumor biopsy, active surveillance, and thermal ablation. *J. Clin Oncology* 36, 36 (December 2018), 3591-3600. <https://www.ncbi.nlm.nih.gov/pmc/articles/PMC6804853/>
- [13] Oleksandr Stakhovskiy, Stanley A. Yap, Michael Leveridge, Nathan Lawrentschuk, and Michael A. S. Jewett. 2011. Small renal mass: what the urologist needs to know for treatment planning and assessment of treatment results. *American Journal of Roengenology* 196, 6 (June 2011), 1243-1467. <https://www.ajronline.org/doi/10.2214/AJR.10.6336>
- [14] John S. Lam, Tobias Klatter, and Alberto Breda. 2009. Staging of renal cell carcinoma: current concepts. *Indian J. of Urol* 25, 4 (October-December 2009), 446-454. <https://doi.org/10.4103%2F0970-1591.57906>
- [15] Michael A. Bruno, Eric A. Walker, and Hani H. Abujudeh. 2015. Understanding and confronting our mistakes: the epidemiology of error in radiology and strategies for error reduction. *Radiographics* 35, 6 (October 2015), 1668-1676. <https://doi.org/10.1148/rq.2015150023>
- [16] Beatriz G. Hidalgo, Juan G. Rivas, Irene de la Parra, María J. Marugán, Álvaro Serrano, Juan F. H. Gutiérrez, et al. 2023. The use of radiomic tools in renal mass characterization. *Diagnostics (Basel)* 13, 17(August 2023), Article Id 2743. <https://doi.org/10.3390/diagnostics13172743>.
- [17] Pei Nie, Guangjie Yang, Zhenguang Wang, Lie Yan, Wenjie Miao, Dapeng Hao, et al. 2020. A CT-based radiomics nomogram for differentiation of renal angiomyolipoma without visible fat from homogeneous clear cell renal cell carcinoma. *Eur Radiol* 30, 2 (February 2020), 1274-1284. <https://doi.org/10.1007/s00330-019-06427-x>
- [18] Nima Nassiri, Marissa Maas, Giovanni Cacciamani, Bino Varghese, Darryl Hwang, Xiaomeng Lei, Monish Aron et al. 2022. A radiomic-based machine learning algorithm to reliably differentiate benign renal masses from renal cell carcinoma. *Eur Urol Focus* 8, 988-994. <https://doi.org/10.1016/j.euf.2021.09.004>
- [19] Igor Frank, Michael L. Blute, John C. Cheville, Christine M. Lohse, Amy L. Weaver, and Horst Zincke. 2003. Solid renal tumors: an analysis of pathological features related to tumor size. *J. Urol* 170, 6-part I (December 2003), 2017-2020. <https://doi.org/10.1097/01.ju.0000095475.12515.5e>
- [20] Andrew B. Rosenkratz, Natasha E. Wehrli, Jonathan Melamed, Samir S. Taneja, and Mohammed B. Shaikh. Renal masses measuring under 2 cm: pathologic outcomes and associations with MRI features. *Eur Radiol* 83 (May 2014), 1311-1316. <https://doi.org/10.1016/j.ejrad.2014.05.016>
- [21] Takayuki Yamada, Mareyuki Endo, Mashahiro Tsuboi, Toshio Matsuhashi, Kei Takase, Shuichi Higano, and Shoki Takahashi. 2008. Differentiation of pathologic subtypes papillary renal cell carcinoma on CT. *AJR* 191 (November 2008), 1559-1563. <https://doi.org/10.2214/AJR.07.3181>
- [22] Dalias Alzu'bi, Malak Abdullah, Ismail Hmeildi, Rami Alazab, Maha Gharaibeh, Mwaffaq El-Heis et al. 2022. Kidney tumor detection and classification based on deep learning approaches. *Journal of Healthcare Engineering* 2022, Article id 3861161. <https://doi.org/10.1155/2022/3861161>
- [23] S. Sudharson and Priyanka Kokil. 2020. An ensemble of deep neural networks for kidney ultrasound image classification. *Computer Methods and Programs in Biomedicine* 197, (December 2020), Article Id 105709. <https://www.sciencedirect.com/science/article/abs/pii/S016926072031542X>
- [24] Fatemeh Zabihollahy, Nicola Schieda, Sateesh Krishna, and Eranga Ukwatta. 2020. Automated classification of solid renal masses on contrast-enhanced computed tomography images using convolutional neural network with decision fusion. *Eur Radiol* 30, 9 (September 2020), 5183–5190. <https://doi.org/10.1007/s00330-020-06787-9>
- [25] Mehmet Erten, Prabal D. Barua, Ilknur Tuncer, Sengul Dogan, Mehmet Baygin, Tucker Tuncer, et al. 2023. Swin-LBP: a competitive feature engineering model for urine sediment classification. *Neural Comp. and Applications* 35, (August 2023), 21621-21632. <https://doi.org/10.1007/s00521-023-08919-w>

- [26] Ze Liu, Yutong Lin, Yue Cao, Han Hu, Yixuan Wei, Zheng Zhang, Stephen Lin, et al. 2021. Swin transformer: hierarchical vision transformer using shifted windows. in Proceedings of the IEEE/CVF International Conference on Computer Vision (ICCV'21), IEEE, Los Alamitos, CA, 10012-10022. <https://doi.org/10.1109/ICCV48922.2021.00986>
- [27] Yu Wu and Zhang Yi. 2020. Automated detection of kidney abnormalities using multi-feature fusion convolutional neural networks. Knowledge-Based Systems 200, (July 2020), Article Id 105873. <https://doi.org/10.1016/j.knosys.2020.105873>
- [28] Hyoung S. Choi, Jare S. Kim, Taeg K. Whangbo, and Sung J. Eun. 2023. Improved detection of urolithiasis using high-resolution computed tomography images by a vision transformer model. Int Neurourol J 27, Suppl 2 (November 2023), S99 - S103. <https://doi.org/10.5213/inj.2346292.146>
- [29] Hyung M. Kim, Seok-Soo Byun, Jung K. Kim, Chang W. Jeong, Cheol Kwak, et al. 2022. Machine learning-based prediction model for late recurrence after surgery in patients with renal cell carcinoma. BMC Medical Informatics and Decision Making 22, 241 (September 2022). <https://link.springer.com/article/10.1186/s12911-022-01964-w>
- [30] Rikiya Yamashita, Mizhuo Nishio, Richard K. G. Do, and Kaori Tagashi. 2018. Convolution neural network: an application of overview in radiology. Insights into Imaging 9, (August 2018), 611-628. <https://doi.org/10.1007/s13244-018-0639-9>
- [31] Ashish Vaswani, Noam Shazeer, Niki Parmar, Jakob Uszkoreit, Llion Jones, Aidan N. Gomez, et al. 2017. Attention is all you need. In Proceedings of the 31st International Conference on Advances in Neural Information Processing Systems (NIPS'17), Curran Associates Inc., Red Hook, NY, 6000-6010. [https://proceedings.neurips.cc/paper\\_files/paper/2017/file/3f5ee243547dee91fb053c1c4a845aa-Paper.pdf](https://proceedings.neurips.cc/paper_files/paper/2017/file/3f5ee243547dee91fb053c1c4a845aa-Paper.pdf)
- [32] Sanghyun Woo, Jongchan Park, Joon-Young Lee, and In S. Kweon. 2018. CBAM: convolutional block attention module. in Proceedings of the European Conference on Computer Vision (ECCV'18). Lecture Notes in Computer Science, Vol. 11129(Part VII), Springer-Verlag, Cham, Switzerland, 3-19. <https://doi.org/10.1007/978-3-030-01234-2>
- [33] Jordon G. Flitcroft, Jeroen Verheyen, Tarun Vemulkar, Emma N. Welbourne, Sabrina H. Rossi, Sarah J. Welsh, et al. 2022. Early detection of kidney cancer using urinary proteins: a truly non-invasive strategy. BJU International 129, 3 (March 2022), 290-303. <https://doi.org/10.1111/bju.15601>
- [34] Sakib Mahmud, Tariq O. Abbas, Adam Mushtak, Joyhra Prithula, and Muhammad E. H. Chowdhary. 2023. Kidney cancer diagnosis and surgery selection by machine learning from CT scans combined with clinical metadata. Cancers 15, 12 (December 2023), Article Id 3189. <https://doi.org/10.3390/cancers15123189>
- [35] Nicholas Heller, Niranjana Sathianathan, Arveen Kalapara, Edward Walczak, Keeman Moore, Heather Kaluzniak et al. 2019. The KiTS19 challenge data: 300 kidney tumor cases with clinical context, CT semantic segmentation, and surgical outcomes. ArXiv. <https://arxiv.org/pdf/1904.00445>
- [36] The 2021 kidney and kidney Tumor Segmentation Challenge. Retrieved July 8, 2024, from <https://kits-challenge.org/kits21/>
- [37] Kaiming He, Xiangyu Zhang, Shaoqing Ren, and Jian Sun. 2016. Deep residual learning for image recognition. In Proceedings of the 29<sup>th</sup> IEEE Conference on Computer Vision and Pattern Recognition (CVPR'16). IEEE, Los Alamitos, CA, 770-778. <https://doi.org/10.1109/CVPR.2016.90>
- [38] Ian T. Jolliffe. 2002. Principal Component Analysis, 2<sup>nd</sup> edition, Springer Series in Statistics, Springer, New York.
- [39] Alexey Dosovitskiy, Lucas Beyer, Alexander Kolesnikov, Dirk Weissenborn, Xiaohua Zhai, Thomas Unterthiner, et al. 2021. An image is worth 16x16 words: transformers for image recognition at scale. In Proceedings of the International Conference on Learning Representations (ICLR '21). ICLR, virtual, <https://openreview.net/pdf?id=YicbFdNTTy>
- [40] Ting-Yun Shiao, Yung-Chang Chang, Hsin-Hung Chou, and Ching-Te Chiu. 2019. Filter based deep-compression with global average pooling for convolution networks. Journal of Systems Architecture 95, (May 2019), 9-18. <https://doi.org/10.1016/j.sysarc.2019.02.008>
- [41] Ramprasaath R. Selvaraju, Michael Cogswell, Abhishek Das, Ramakrishna Vedantam, Devi Parikh, and Dhruv Batra. 2017. Grad-CAM: visual explanations from deep networks via gradient-based localization. In Proceedings of the IEEE International Conference on Computer Vision (ICCV'17), IEEE, Los Alamitos, CA, 618-626. <https://doi.org/10.1109/ICCV.2017.74>
- [42] Nitesh V. Chawla, Kevin W. Bowyer, Lawrence O. Hall, and W. Philip Kegelmeyer. 2002. SMOTE: synthetic minority over-sampling technique. J. Artif. Int. Res. 16, 1 (June 2002), 321-357. <https://dl.acm.org/doi/10.5555/1622407.1622416>
- [43] Kwang-Hyun Uhm, Seung-Won Jung, Moon H. Choi, Hong-Kyu Shin, Jae-Ik Yoo, Se W. Oh, Jee Y. Kim, et al. 2021. Deep learning for end-to-end kidney cancer diagnosis on multi-phase abdominal computed tomography. NPJ Precision Oncology 5, (June 2021), Article Id 54. <https://doi.org/10.1038/s41698-021-00195-y>